A Global Database of Strong-Motion Displacement GNSS Recordings and an Example Application to PGD Scaling

by Christine J. Ruhl, Diego Melgar, Jianghui Geng, Dara E. Goldberg, Brendan W. Crowell, Richard M. Allen, Yehuda Bock, Sergio Barrientos, Sebastian Riquelme, Juan Carlos Baez, Enrique Cabral-Cano, Xyoli Pérez-Campos, Emma M. Hill, Marino Protti, Athanassios Ganas, Mario Ruiz, Patricia Mothes, Paul Jarrín, Jean-Mathieu Nocquet, Jean-Phillipe Avouac, and Elisabetta D'Anastasio

ABSTRACT

Displacement waveforms derived from Global Navigation Satellite System (GNSS) data have become more commonly used by seismologists in the past 15 yrs. Unlike strong-motion accelerometer recordings that are affected by baseline offsets during very strong shaking, GNSS data record displacement with fidelity down to 0 Hz. Unfortunately, fully processed GNSS waveform data are still scarce because of limited public availability and the highly technical nature of GNSS processing. In an effort to further the use and adoption of high-rate (HR) GNSS for earthquake seismology, ground-motion studies, and structural monitoring applications, we describe and make available a database of fully curated HR-GNSS displacement waveforms for significant earthquakes. We include data from HR-GNSS networks at near-source to regional distances (1–1000 km) for 29 earthquakes between M_w 6.0 and 9.0 worldwide. As a demonstration of the utility of this dataset, we model the magnitude scaling properties of peak ground displacements (PGDs) for these events. In addition to tripling the number of earthquakes used in previous PGD scaling studies, the number of data points over a range of distances and magnitudes is dramatically increased. The data are made available as a compressed archive with the article.

INTRODUCTION

Over the past decade and a half, displacements from high-rate (HR, sampling rate ≥ 1 samples/s) Global Navigation Satellite System (GNSS) data, specifically from Global Positioning System (GPS), have become a more common measurement in seismology. GNSS is a fundamentally different sensing platform from the inertial seismometers more commonly used. It relies on travel-time measurements of electromagnetic waves from a GNSS antenna to a constellation of satellites with precisely known orbits. Geodetic analysis of the multifrequency GNSS data produces reliable and unsaturated measurements of ground-motion displacement from 0 Hz (the static offset or permanent deformation) to the Nyquist frequency introduced by the GNSS sampling rate.

Because strong motion sensors are affected by baseline offsets, a different measuring device is needed. These offsets are small errors introduced into acceleration time series during strong shaking. Their precise nature is a matter of debate, and a review of the physics behind them can be found in Boore (2001). Whatever their physical source, baseline offsets are unavoidable in inertial systems, and they make long-period measurements of ground motion unreliable.

To ameliorate this issue, it is possible to use measurements from HR-GNSS. Because GNSS is noninertial and directly measures displacements in an absolute global reference frame—that of the Earth—it is not subject to baseline offsets. HR-GNSS is reliable at long periods down to the static offset but has higher noise levels than strong-motion sensors, usually ~1–2 cm. Thus, they are only useful for moderate to large events and at local to regional distances.

As a result, the use of HR-GNSS data has become more and more widespread. Perhaps it is most widely used in earthquake source studies in which it is usually inverted on its own or jointly with other geophysical datasets to image the kinematic source process of M_w 6+ events, which generate displacements large enough to be above the GNSS noise level. HR-GNSS has also been used in studies of long-period ground motions and in structural monitoring. A review of the evolution, uses, and algorithms behind HR-GNSS can be found in Bock and Melgar (2016).

Despite this rapid evolution to becoming a mainstream tool in seismology, a fundamental challenge to a more widespread

Downloaded from https://pubs.geoscienceworld.org/ssa/srl/article-pdf/90/1/271/4602961/srl-2018177.1.pdf
by University of California Berkeley Library, rallen

adoption of HR-GNSS remains. There is scarcity of fully processed displacement waveforms for large events in a central repository. Converting the raw GNSS observables (phase and range measurements of the electromagnetic waves) to displacements is out of technical reach of most seismologists. Additionally, although several countries operate national GNSS networks, many of them have a closed data policy. It is not always straightforward to gain access to data either in real time or soon after an event. Furthermore, when a research group does acquire raw GNSS data and produce displacement waveforms, they are not collected in a centralized repository (e.g., the Incorporated Research Institution for Seismology), nor processed in a uniform way. It is true that there are repositories of raw GNSS data such as UNAVCO and the Scripps Orbit and Permanent Array Center, but even here there is no mechanism for archiving fully processed HR displacement waveforms in a concerted fashion and in formats readily usable by seismologists and engineers.

In an effort to promote the use and adoption of HR-GNSS for earthquake seismology, ground-motion studies, earthquake engineering, and structural monitoring applications, in this article, we describe and make open a database of HR-GNSS displacement waveforms that the authors have collected over the past 15 yrs (see Data and Resources for download instructions). The database consists of 3433 three-component HR-GNSS recordings (10,299 individual waveforms) of ground motion processed in a coherent way using the algorithm described by Geng *et al.* (2013). The data are presented in a unified and well-described seismic format (miniSEED) with accompanying metadata. As a demonstration of the utility of the database, we also produce a peak ground displacement (PGD) scaling law to update the ones provided by Crowell *et al.* (2013, 2016) and Melgar *et al.* (2015).

GLOBAL DATASET

The dataset consists of HR-GNSS observations for 29 large ($M_w \geq 6$) earthquakes worldwide (Table 1 and Fig. 1). The overwhelming majority of the recordings are collected at 1 Hz, but a few (2010 M_w 7.2 El Mayor–Cucapah, 2012 M_w 7.6 Nicoya, 2014 M_w 6.1 Napa, and 2015 M_w 7.8 Nepal) have some 5-Hz recordings. We processed the raw observations with a precise point positioning algorithm (Geng *et al.*, 2013) to obtain displacement time series in geodetic coordinates. Undifferenced GNSS ambiguities were fixed to integers to improve the displacement accuracy, especially over the low-frequency band of tens of seconds (Geng *et al.* 2017). We then rotate the coordinates to a local north–south, east–west, and up–down system, similar to what is provided in most free-field seismic recordings.

The events range in magnitude from 2004 M_w 6.0 Parkfield to 2011 M_w 9.0 Tohoku-oki. The database is dominated by subduction zone megathrust events but includes continental strike-slip (e.g., 2016 M_w 7.0 Kumamoto), intraplate normal (e.g., 2017 M_w 8.2 Tehuantepec), and other nonsubduction zone events. All events have hypocenters shallower than 60 km, and the number of stations available for each event varies widely. Some have only a few sites such as the M_w 7.8 Nepal earthquake, which has only seven stations. Others, such as the M_w 9.0 Tohoku-oki earthquake, have more than 800.

Finally, because GNSS data are noisy, stations farther from the source for some of the more moderate magnitude events do not record any meaningful signals. We applied criteria to rule out such waveforms. We calculate the signal-to-noise ratio (SNR) for all the waveforms and include only those with SNR ≥ 3. Also, because the noise level in GNSS is known and somewhat constant, we apply an arbitrary minimum amplitude cutoff. We only retain waveforms with peak amplitudes larger than or equal to 4 cm. After these filters are applied, we are left with the 3433 three-component HR-GNSS recordings.

The data are structured as follows. There is one large tarball available for download on Zenodo (see Data and Resources). Inside the archive, there is one folder per event clearly labeled with the names in Table 1. Inside each event folder is a text file (EVENT_disp.chan) with station metadata (station codes and coordinates). There is a "disp" folder, which contains files named using the convention STA.LXE.mseed, STA.LXN.mseed, and STA.LXZ.mseed in which STA is the station code and LXE, LXN, and LXZ are east, north, and up waveforms, respectively. The sampling rate for each waveform is indicated inside the miniSEED header of each waveform as well as in the channel file. The data are provided in UTC time with leap seconds fully corrected for (GNSS data are time-tagged in GPS time, which is not corrected for leap seconds).

AN EXAMPLE APPLICATION: PEAK GROUND DISPLACEMENT SCALING

Background and Method

The source scaling of PGD was first noted by Crowell *et al.* (2013) from observations of the M_w 9.0 Tohoku-Oki, M_w 8.3 Tokachi-Oki, and M_w 7.2 El Mayor–Cucapah earthquakes. Later, Melgar *et al.* (2015) expanded the observational data to 10 moderate to large events by producing another PGD scaling law and proposing a simple algorithm for its real-time use as an unsaturated estimator of magnitude. Here, we updated that PGD scaling law with the complete database of 29 events.

The method is as follows. We calculate PGD as

$$\mathrm{PGD}_j^i = \max\left(\sqrt{[N(t)^2 + E(t)^2 + U(t)^2]}\right), \tag{1}$$

for the *i*th station and *j*th earthquake. We then use the functional form for the scaling law proposed by Crowell *et al.* (2013), which includes magnitude-dependent attenuation to account for the relative strengths of the near-, intermediate-, and far-field seismic radiation terms such that

$$\log(\mathrm{PGD}) = A + B \times M_w + C \times M_w \times \log(R), \tag{2}$$

in which A, B, and C are the regression coefficients; M_w is the known moment magnitude for the earthquake from the Global Centroid Moment Tensor catalog (see Data and Resources); and R is the source to station distance. Here, we measure

Downloaded from https://pubs.geoscienceworld.org/ssa/srl/article-pdf/90/1/271/4602961/srl-2018177.1.pdf
by University of California Berkeley Library, rallen

Table 1
Details of the 29 Earthquakes Used in This Study

	Event Name, Country	Origin Time (UTC)	Longitude (°)	Latitude (°)	Depth (km)	M_w	Number of Stations	Mechanism
1	Tohoku2011, Japan	2011-03-11T05:46:24	142.3720	38.2970	30.0	9.0	812	Reverse
2	Maule2010, Chile	2010-02-27T06:34:14	−72.7330	−35.9090	35.0	8.8	20	Reverse
3	Illapel2015, Chile	2015-09-16T22:54:33	−71.6540	−31.5700	29.0	8.3	38	Reverse
4	Tokachi2003, Japan	2003-09-25T19:50:06	143.9040	41.7750	27.0	8.3	346	Reverse
5	Tehuantepec2017, Mexico	2017-09-08T04:49:19	−93.8990	15.0220	47.4	8.2	7	Normal
6	Iquique2014, Chile	2014-04-01T23:46:47	−70.7690	−19.6100	25.0	8.1	23	Reverse
7	Ecuador2016, Ecuador	2016-04-16T23:58:36	−79.9220	0.3820	20.6	7.8	21	Reverse
8	Kaikoura2016, New Zealand	2016-11-13T11:02:56	173.0540	−42.7370	15.0	7.8	36	Strike slip
9	Nepal2015, Nepal	2015-04-25T06:11:25	84.7310	28.2310	8.2	7.8	7	Reverse
10	Ibaraki2011, Japan	2011-03-11T06:15:34	141.2653	36.1083	43.2	7.7	709	Reverse
11	Iquique_aftershock2014, Chile	2014-04-03T02:43:13	−70.4930	−20.5710	22.4	7.7	12	Reverse
12	Mentawai2010, Indonesia	2010-10-25T14:42:22	100.1140	−3.4840	20.0	7.7	12	Reverse
13	N.Honshu2011, Japan	2011-03-11T06:25:44	144.8940	37.8367	34.0	7.7	150	Normal
14	Melinka2016, Chile	2016-12-25T14:22:26	−74.3910	−43.5170	30.0	7.6	7	Reverse
15	Nicoya2012, Costa Rica	2012-09-05T14:42:08	−85.3050	10.0860	40.0	7.6	9	Reverse
16	Iwate2011, Japan	2011-03-11T06:08:53	142.7815	39.8390	31.7	7.4	200	Reverse
17	Miyagi2011A, Japan	2011-03-09T02:45:12	143.2798	38.3285	8.3	7.3	186	Reverse
18	N.Honshu2012, Japan	2012-12-07T08:18:20	144.3153	37.8158	46.0	7.3	104	Reverse
19	Nepal_aftershock2015, Nepal	2015-05-12T07:05:19	86.0660	27.8090	15.0	7.3	5	Reverse
20	ElMayor2010, Mexico	2010-04-04T22:40:42	−115.2800	32.2590	10.0	7.2	93	Strike slip
21	Miyagi2011B, Japan	2011-04-07T14:32:43	141.9237	38.2028	60.7	7.1	198	Reverse
22	N.Honshu2013, Japan	2013-10-25T17:10:18	144.5687	37.1963	56.0	7.1	9	Reverse
23	Puebla2017, Mexico	2017-09-19T18:14:38	−98.4890	18.5500	48.0	7.1	5	Normal
24	Kumamoto2016, Japan	2016-04-15T16:25:05	130.7630	32.7545	12.5	7.0	229	Strike slip
25	Aegean2014, Greece	2014-05-24T09:25:02	25.3890	40.2890	12.0	6.9	4	Strike slip
26	E.Fukushima2011, Japan	2011-04-11T08:16:12	140.6727	36.9457	6.4	6.6	107	Normal
27	Lefkada2015, Greece	2015-11-17T07:10:07	20.6002	38.6650	10.7	6.5	5	Strike slip
28	Napa2014, U.S.A.	2014-08-24T10:20:44	−122.3100	38.2150	11.0	6.1	67	Strike slip
29	Parkfield2004, U.S.A.	2004-09-28T17:15:24	−120.3700	35.8150	7.9	6.0	12	Strike slip

PGD in meters as seen in Figure 2. For every station–event pair, we compute the hypocentral distance R, which accounts for the depth of the event, using the hypocenter location determined by the National Earthquake Information Center (see Data and Resources).

Because the data points are unevenly distributed (Fig. 2), with more data at the lower magnitudes and larger source-to-station distances, we introduce a weighting scheme that removes this bias. We separate the data into 20 bins each in $\log(R)$ and in $\log(\mathrm{PGD})$, effectively dividing the 2D space spanned by $\log(\mathrm{PGD})$ and $\log(R)$ into 400 discrete bins. For each bin, we introduce a weight w_k defined as

$$w_k = \log\left(\frac{1}{\sum_{k=0}^{n} \mathrm{PGD}_k}\right), \quad (3)$$

in which PGD_k is the PGD measurement in meters in a particular bin. We use the sum of actual values. This weighting scheme ensures that all parts of the $\log(\mathrm{PGD})$ versus $\log(R)$ space are given equal importance in the regression. After the weights are applied, we conduct a linear weighted least-squares regression to estimate the coefficients A, B, and C.

RESULTS AND DISCUSSION

Our estimated coefficients are shown in Table 2 and compared with those previously obtained by Melgar *et al.* (2015) and Crowell *et al.* (2016). Figure 3 shows the differences between observed PGD and predicted PGD for the scaling law derived here and for those of Melgar *et al.* (2015) and Crowell *et al.* (2016).

Downloaded from https://pubs.geoscienceworld.org/ssa/srl/article-pdf/90/1/271/4602961/srl-2018177.1.pdf
by University of California Berkeley Library, rallen

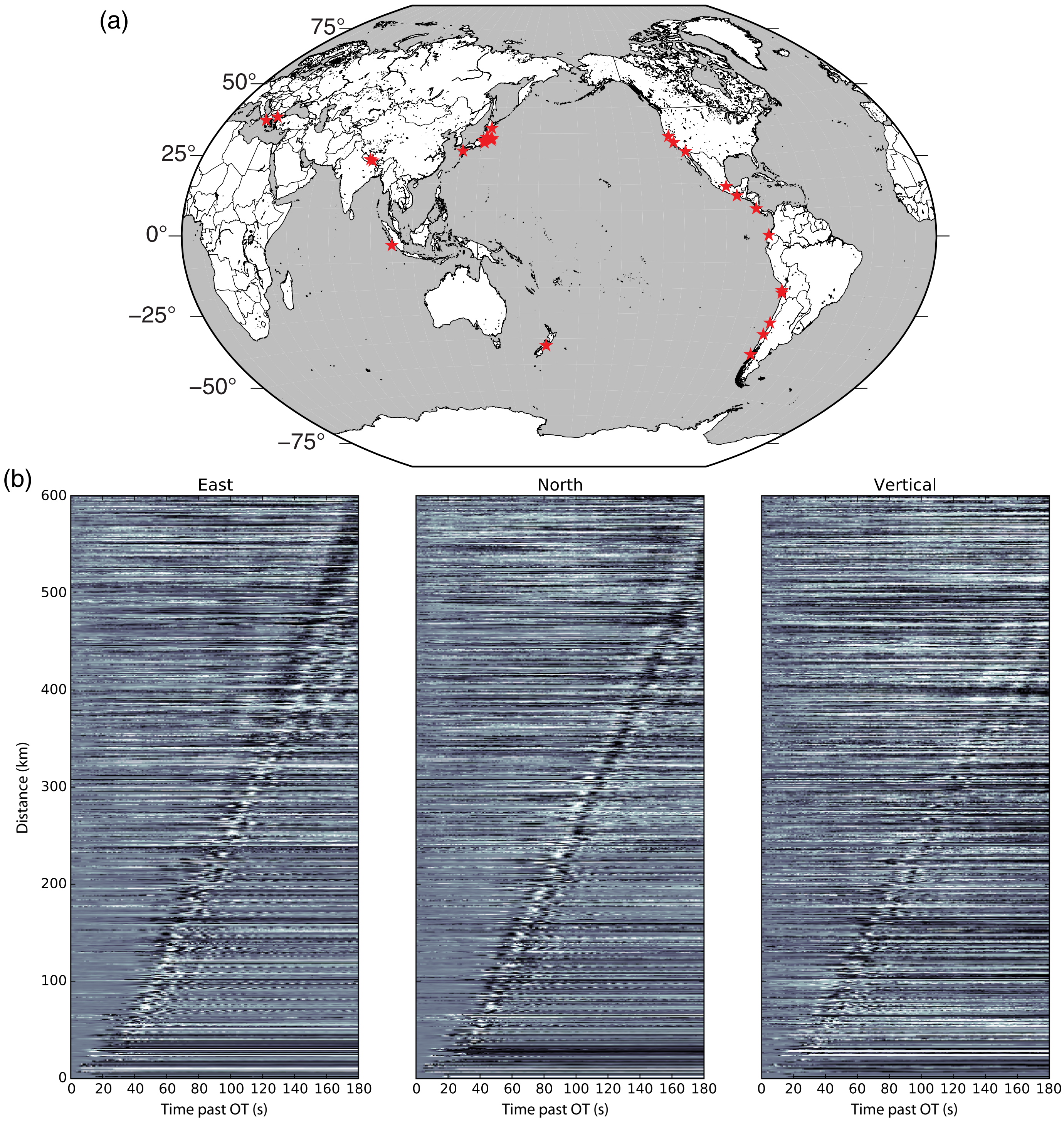

▲ **Figure 1.** (a) Map of 29 earthquakes and (b) three-component displacement waveforms within 600 km hypocentral distance for all 29 earthquakes. The color version of this figure is available only in the electronic edition.

To further understand the results of the regression, we calculated the PGD residuals (ϱ_i) as the natural log of the ratio of the prediction of the regression (pred_i) and the observed PGD (obs_i) such that:

$$\varrho_i = \ln(\text{obs}_i/\text{pred}_i). \tag{4}$$

PGD measurements are shaded by residual in Figure 4. In Figure 5, we disaggregated the residuals by magnitude and distance. Here, we see that although individual events can have an overall positive or negative bias, there is no overall magnitude bias in the scaling law. This is due to the chosen weighting scheme (equation 3). However, why an individual event devi-

Downloaded from https://pubs.geoscienceworld.org/ssa/srl/article-pdf/90/1/271/4602961/srl-2018177.1.pdf
by University of California Berkeley Library, rallen

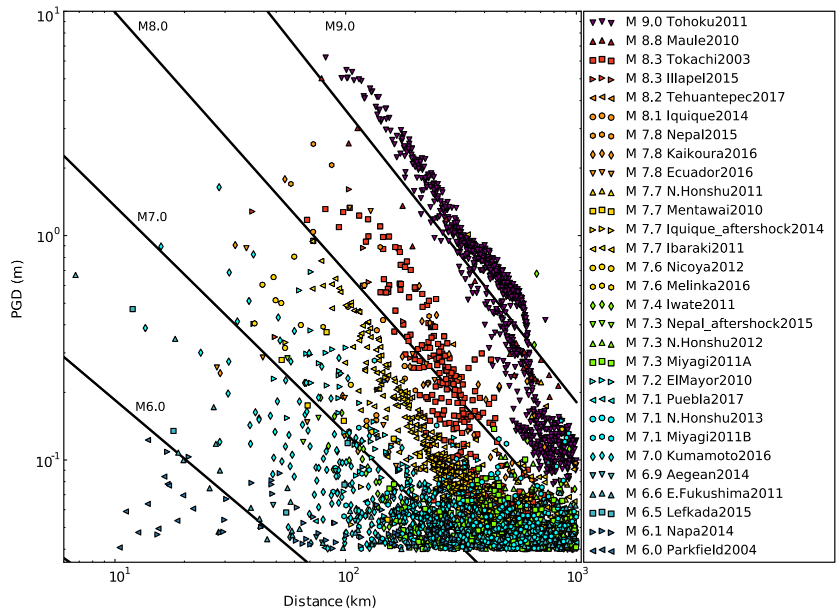

▲ **Figure 2.** Peak ground displacement (PGD) measurements with hypocentral distance. Oblique lines are the predicted scaling values from the least-squares regression of the PGD measurements as a function of hypocentral distance. The color version of this figure is available only in the electronic edition.

ates from the trend is also interesting. It could be because of higher or lower stress drops, but little is known about how these affect PGD. Similarly, it could be because of path or site effects. Likewise, little is known about how these affect PGD.

The PGD versus distance plot also shows an interesting trend. It is clear that there is a distance dependence to the residuals. At short distances, the scaling law overpredicts the observed PGD. We posit that this is because the current functional form of the scaling law (equation 2) is too simple. At the limit where distance is zero, it predicts an infinitely large PGD that is not physically realistic. One would expect that as the source–station distances become smaller, PGD should approximate the local slip on the portion of the fault closest to the site; it should not grow unbounded with decreasing distance. This is not currently captured in any of the existing PGD scaling laws.

Table 2
Comparison of Peak Ground Displacement (PGD) Scaling Law Coefficients from This Study, Melgar *et al.* (2015), and Crowell *et al.* (2016)

A	*B*	*C*	Origin
−5.919	1.009	−0.145	This study
−4.434	1.047	−0.138	Melgar *et al.* (2015)
−6.687	1.500	−0.214	Crowell *et al.* (2016)

We have used PGD in meters, but Melgar *et al.* (2015) and Crowell *et al.* (2016) used PGD in centimeters.

We summed the residuals from all observations to obtain the total residual. For the scaling law derived here, the total residual has a comparable value (1750) to that obtained from the Melgar *et al.* (2015) scaling law (1747). It is substantially better than the total residual using the Crowell *et al.* (2016) scaling law (2724). Taking into account that the magnitude and distance biases are smaller with the scaling law derived here, it should be considered a more authoritative representation of the behavior of PGD. However, much research is left to do as more and more events are recorded by GNSS networks. For now, the outcome is simply a scaling law that is objectively better than those previously published.

OTHER POTENTIAL USES OF HR-GNSS AND FUTURE OUTLOOK

PGD scaling has been adopted by rapid source characterization algorithms because it is an easy to calculate real-time metric that does not saturate (e.g., Crowell *et al.*, 2016); however, we suggest that there are other as yet to be exploited uses of GNSS, particularly in ground-motion studies. For example, Kamai and Abrahamson (2015) noted that near-fault fling effects are not well modeled by currently existing ground-motion prediction equations (GMPEs). Fling, in the near field, is the superposition of the static offset and the PGD resulting from a propagating slip pulse at the source. Although it was concluded in that study that this shortcoming did not affect higher frequency ground-motion metrics such as peak ground acceleration, it is clear that for large engineered structures that would be most affected by this, the current characterization of displacements is quite limited in modern GMPEs.

Thus, we contend that GNSS displacements from databases such as this one could be of use for GMPE developers. For example, Melgar *et al.* (2013) showed by an analysis of collocated GNSS and strong-motion sites for the M_w 9.0 Tohoku-Oki earthquake that at periods longer than 10 s the ground motions recorded by the strong-motion sensor, even after careful and objective baseline correction, could be substantially biased. More worryingly, in the absence of external measurements from geodesy, this bias would not be easily recognized. The baseline-corrected waveforms may look physically reasonable but could be in large error both in the peak amplitudes and in the final static offset. A systematic comparison of spectral accelerations (SAs) predicted by GMPEs versus SAs from strong-motion recordings and from GNSS recordings has not yet been made. It should be possible to determine by such a comparison whether such long-period biases are more widespread.

Recordings of ground-motion displacement close to large earthquakes have been used to supplement other geophysical

Downloaded from https://pubs.geoscienceworld.org/ssa/srl/article-pdf/90/1/271/4602961/srl-2018177.1.pdf
by University of California Berkeley Library, rallen

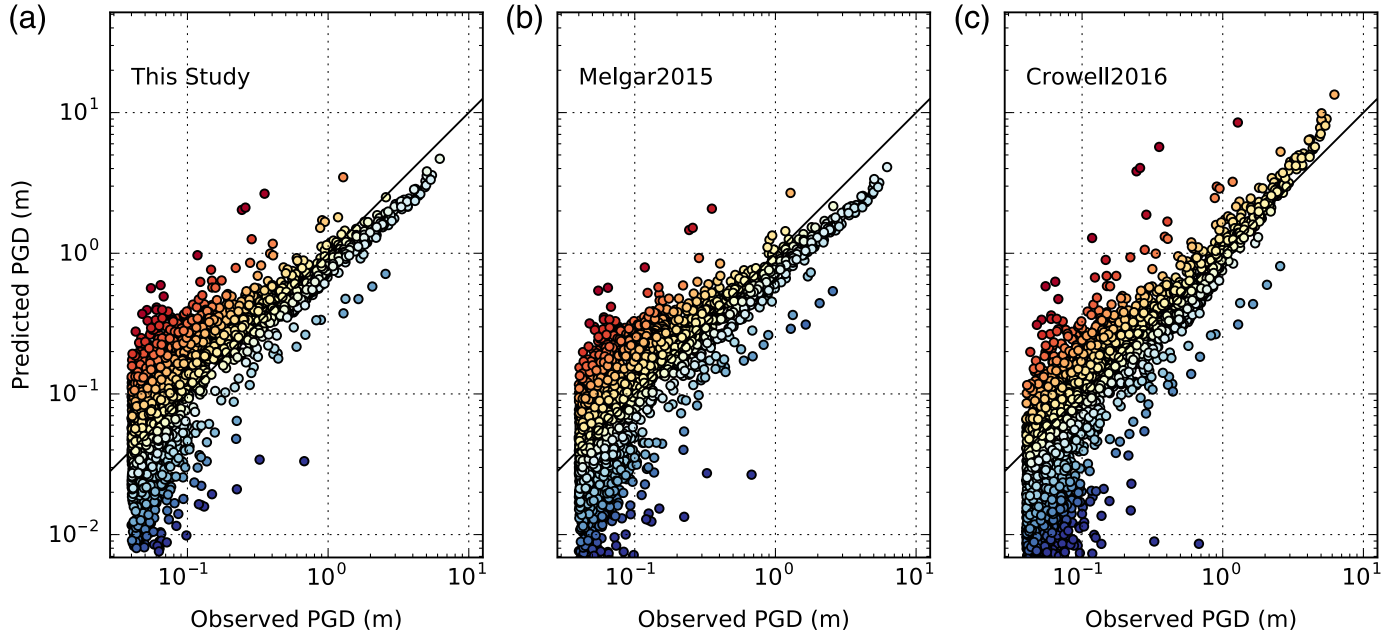

▲ **Figure 3.** Predicted versus observed PGD for the coefficients found in (a) this study, (b) Melgar *et al.* (2015), and (c) Crowell *et al.* (2016). The color version of this figure is available only in the electronic edition.

observables when producing inverse models of source kinematics (e.g., Lay, 2017; Satake and Heidarzadeh, 2017). HR-GNSS waveforms are important because they give excellent long-period constraints on total moment and slip. For example, Riquelme *et al.* (2016) have shown that HR-GNSS displacements can be used for W-phase moment inversion of large events at closer distances than broadband seismic recordings. Additionally, HR-GNSS waveforms have recently been used in debates about large earthquake dynamics (Melgar and Hayes, 2017; Goldberg *et al.*, 2018), specifically with regard to the nature of early moment release and to whether this has implications for rupture determinism (e.g., Meier *et al.*, 2017). We hope that by making these waveforms available, such studies will continue, and perhaps a synthesis will be made on what GNSS recordings reveal about the earthquake source process.

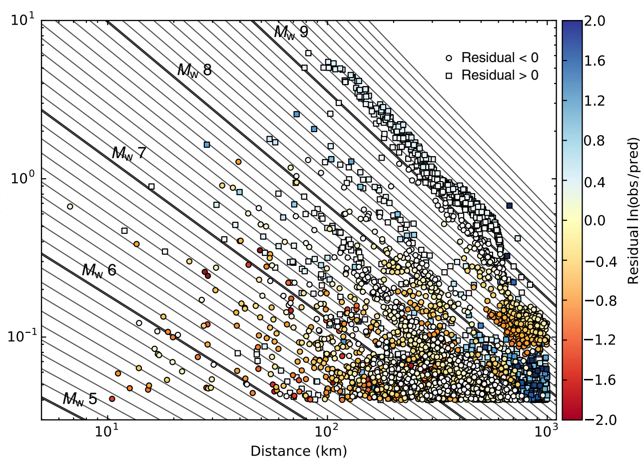

▲ **Figure 4.** PGD measurements with hypocentral distance colored by residual. Circles are negative residuals, and squares are positive residuals. Oblique lines are the predicted scaling values from the least-squares regression of the PGD measurements as a function of hypocentral distance. The color version of this figure is available only in the electronic edition.

Importantly, HR-GNSS is playing an expanding role in earthquake early warning. In the United States, the ShakeAlert system (Given *et al.*, 2014) is testing numerous prototype codes that use GNSS for real-time source characterization (Grapenthin *et al.*, 2014; Minson *et al.*, 2014; Crowell *et al.*, 2016). Research is ongoing to understand when, within a potentially minutes-long rupture process, such products provide useful estimates of strong shaking (Ruhl *et al.*, 2017). We hope that databases such as this one will be used to test new generations of algorithms that incorporate still-developing scientific findings on the issue of rupture determinism.

Likewise, for local tsunami early warning, HR-GNSS has a critical role to play. In addition to rapid unsaturated magnitude estimates from PGD, HR-GNSS provides rapid focal mechanisms and slip inversions (Crowell *et al.*, 2016). These can be used to forecast tsunami amplitudes at the near-shore coast 2–3 min after an earthquake's onset (Melgar *et al.*, 2016). These approaches are slowly becoming operational at monitoring agencies such as National Oceanic and Atmospheric Administration's tsunami warning centers. Nonetheless, numerous research problems still exist. For example, how can HR-GNSS be used to identify shallow and highly tsunamigenic slip? We hope the data will aid in such research.

Finally, we note that although throughout this article, we referred to GNSS, the displacements calculated and made available here were obtained from processing only observations

Downloaded from https://pubs.geoscienceworld.org/ssa/srl/article-pdf/90/1/271/4602961/srl-2018177.1.pdf
by University of California Berkeley Library, rallen

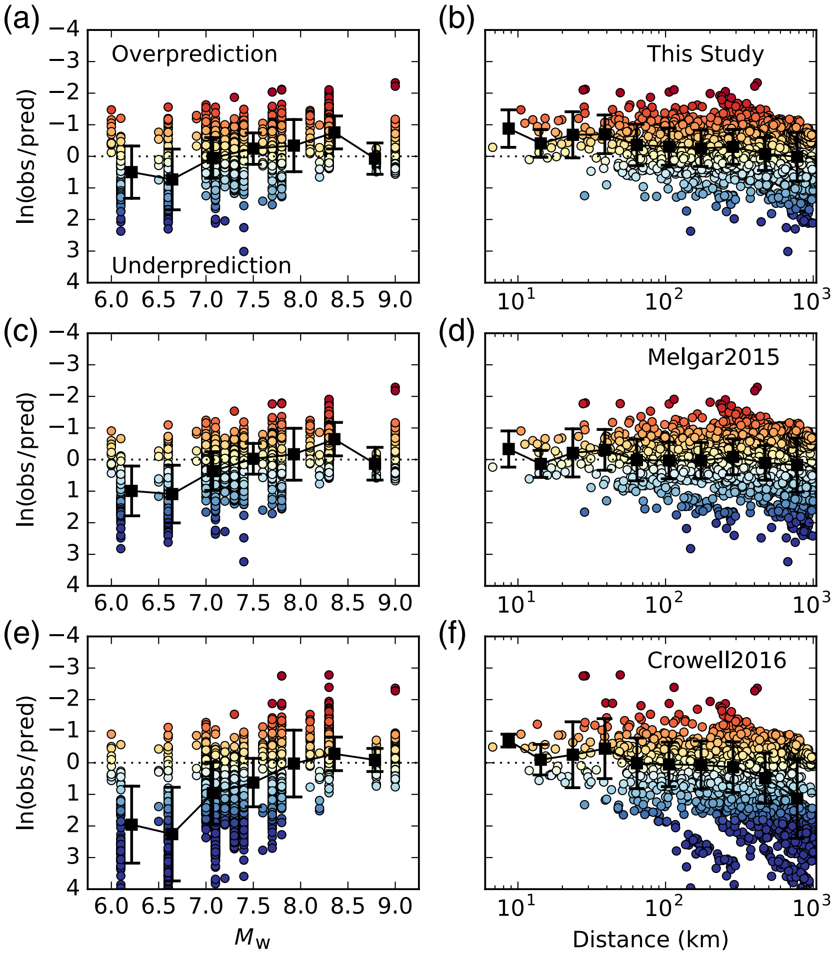

▲ **Figure 5.** Residuals plotted (a) as a function of earthquake magnitude and (b) as a function of hypocentral distance for PGD–magnitude scaling laws derived (top row) in this study, (middle row) by Melgar *et al.* (2015), and (bottom row) by Crowell *et al.* (2016). Medians (black squares) with one standard deviation error bars are shown. The color version of this figure is available only in the electronic edition.

of the GPS constellation of satellites. Networks and processing algorithms that capture the full benefits of multiconstellation observations (true GNSS) are not yet the norm. However, research clearly shows that full GNSS HR positions offer better accuracy over GPS-only solutions (Geng *et al.*, 2018) as well as fewer artifacts and faster reconversion after signal loss. As this new paradigm becomes the norm, waveforms from our database can be used as signpost to measure improvements.

CONCLUSIONS

To further the inclusion and access of HR-GNSS for earthquake seismology, ground-motion studies, early warning systems, and structural monitoring applications, we describe and make available a database of fully curated HR-GNSS displacement waveforms for 29 earthquakes between M_w 6.0 and 9.0 around the world. We include data from HR-GNSS networks at near-source to regional distances (1–1000 km) with SNR ≥ 3 and PGD ≥ 4 cm. In addition to tripling the number of earthquakes used in previous PGD scaling studies, the number of data points over a range of distances and magnitudes is dramatically increased. We improve the magnitude scaling properties of PGD for these events as a demonstration. We find similar coefficients to Melgar *et al.* (2015) that are well fit over the magnitude and distance ranges used. This dataset is valuable to earthquake seismologists and engineers, and we hope to encourage and facilitate the incorporation of GNSS data into earthquake studies moving forward.

DATA AND RESOURCES

We provide a compressed file that includes directories of processed miniSEED displacement data for all 29 events as well as record section plots of all 29 events. These data are permanently stored at https://zenodo.org/record/1434374. There are two versions of the dataset at that link; version 2.0 should be considered authoritative and contains only stations with signal-to-noise ratio (SNR) > 3 and peak ground displacement (PGD) > 4 cm. Version 1.0 contains all data, including those sites that only recorded noise. Global Centroid Moment Tensor (CMT) data came from http://globalcmt.org, and National Earthquake Information Center (NEIC) data came from http://earthquake.usgs.gov. Chilean data are from the Centro Sismológico Nacional at the Universidad de Chile. High-rate RINEX files can be downloaded at http://gps.csn.uchile.cl/data. Data from Greece is from the National Observatory of Athens which operates the NOANET Global Navigation Satellite System (GNSS) network, which also incorporates data from SMARTnet (Greece) and KOERI stations in Turkey. For Mexico, this material is based on data provided by Servicio Sismologico Nacional (SSN), SSN-TLALOCNet, and TLALOCNet GPS networks, operated by SSN and Servicio de Geodesia Satelital (SGS) at Instituto de Geofísica-Universidad Nacional Autónoma de México (UNAM) and UNAVCO Inc. and supported by National Science Foundation (NSF) EAR-1338091, Consejo Nacional de Ciencia y Tecnologia (CONACyT) Infraestructura 253760, CONACyT Problemas Nacionales 5955, and UNAM-Proyectos de Investigación e Innovación Tecnológica (PAPIIT) projects IN104213, IN109315-3, IA101913, and IA100916. TLALOCNet raw data are available at http://tlalocnet.udg.mx. Ecuador data are from the National Geodetic Network of the Instituto Geofisico of the Escuela Politecnica Nacional (RENGEO). This network has been funded by Secretaria de Educacion Superior, Ciencia Tecnologia, e Inovacion (SENASCYT) PIN-08-EPNGEO-001 project and Secretaria Nacional de Planificacion y Desarrolo-Escuela Politecnica Nacional (SENPLADES-EPN's) Generación de capacidades

Downloaded from https://pubs.geoscienceworld.org/ssa/srl/article-pdf/90/1/271/4602961/srl-2018177.1.pdf
by University of California Berkeley Library, rallen

para la difusión de alertas tempranas project. Data from Indonesia are from the Sumatran GPS Array (SuGAr), which is operated and maintained by the Earth Observatory of Singapore and the Indonesian Institute of Sciences (LIPI). All websites were last accessed on September 2018.

ACKNOWLEDGMENTS

The authors thank Ronni Grapenthin and Valerie Sahakian for helpful discussions on the peak ground displacement (PGD) scaling law and residuals. This work was funded by the Gordon and Betty Moore Foundation through Grant GBMF3024 to University of California (UC) Berkeley and the U.S. Geological Survey Grants G16AC00348 and G17AC00346 to UC Berkeley. Work was also done under Grant 41674033 from the National Science Foundation of China. Scripps Orbit and Permanent Array Center (SOPAC) work was funded by NASA Grants NNH17ZDA001N, NNX16AM04A and NNX17AD99G and National Science Foundation (NSF) Grant EAR-1400. The authors thank the Geospatial Information Authority of Japan for operation and maintenance of the GEONET Global Positioning System (GPS) network whose data are used in this study. The authors gratefully acknowledge all the personnel from Servicio Sismologico Nacional (SSN), Servicio de Geodesia Satelital (SGS) and UNAVCO Inc. for GPS station maintenance, data acquisition, IT support and data distribution. The authors acknowledge the New Zealand GeoNet project and its sponsors EQC, GNS Science, and LINZ, for providing data used in this study.

REFERENCES

Bock, Y., and D. Melgar (2016). Physical applications of GPS geodesy: A review, *Rep. Progr. Phys.* **79,** no. 10, 106801.

Boore, D. M. (2001). Effect of baseline corrections on displacements and response spectra for several recordings of the 1999 Chi-Chi, Taiwan, earthquake, *Bull. Seismol. Soc. Am.* **91,** no. 5, 1199–1211.

Crowell, B. W., D. Melgar, Y. Bock, J. S. Haase, and J. Geng (2013). Earthquake magnitude scaling using seismogeodetic data, *Geophys. Res. Lett.* **40,** 6089–6094, doi: 10.1002/2013GL058391.

Crowell, B. W., D. A. Schmidt, P. Bodin, J. E. Vidale, J. Gomberg, J. Renate Hartog, V. C. Kress, T. I. Melbourne, M. Santillan, S. E. Minson, *et al.* (2016). Demonstration of the Cascadia G-FAST geodetic earthquake early warning system for the Nisqually, Washington, earthquake, *Seismol. Res. Lett.* **87,** no. 4, 930–943.

Geng, J., Y. Bock, D. Melgar, B. W. Crowell, and J. S. Haase (2013). A new seismogeodetic approach applied to GPS and accelerometer observations of the 2012 Brawley seismic swarm: Implications for earthquake early warning, *Geochem. Geophys. Geosys.* **14,** no. 7, 2124–2142.

Geng, J., P. Jiang, and J. Liu (2017). Integrating GPS with GLONASS for high-rate seismogeodesy, *Geophys. Res. Lett.* **44,** no. 7, 3139–3146, doi: 10.1002/2017GL072808.

Geng, J., Y. Pan, X. Li, J. Guo, J. Liu, X. Chen, and Y. Zhang (2018). Noise characteristics of high-rate multi-GNSS for subdaily crustal deformation monitoring, *J. Geophys. Res.* **123,** no. 2, 1987–2002.

Given, D. D., E. S. Cochran, T. Heaton, E. Hauksson, R. Allen, P. Hellweg, J. Vidale, and P. Bodin (2014). Technical implementation plan for the ShakeAlert production system: An earthquake early warning system for the West Coast of the United States, *U.S. Geol. Surv. Open-File Rept. 2014-1097*, 25 pp.

Grapenthin, R., I. A. Johanson, and R. M. Allen (2014). Operational real-time GNSS-enhanced earthquake early warning, *J. Geophys. Res.* **119,** 7944–7965, doi: 10.1002/2014JB011400.

Kamai, R., and N. Abrahamson (2015). Are near-fault fling effects captured in the new NGA West2 ground motion models?, *Earthq. Spectra* **31,** no. 3, 1629–1645.

Lay, T. (2017). A review of the rupture characteristics of the 2011 Tohoku-oki M_w 9.1 earthquake, *Tectonophysics* **733,** 4–36, doi: 10.1016/j.tecto.2017.09.022.

Meier, M. A., J. P. Ampuero, and T. H. Heaton (2017). The hidden simplicity of subduction megathrust earthquakes, *Science* **357,** no. 6357, 1277–1281.

Melgar, D., and G. P. Hayes (2017). Systematic observations of the slip pulse properties of large earthquake ruptures, *Geophys. Res. Lett.* **44,** no. 19, 9691–9698.

Melgar, D., R. M. Allen, S. Riquelme, J. Geng, F. Bravo, J. C. Baez, H. Parra, S. Barrientos, P. Fang, Y. Bock, *et al.* (2016). Local tsunami warnings: Perspectives from recent large events, *Geophys. Res. Lett.* **43,** no. 3, 1109–1117.

Melgar, D., Y. Bock, D. Sanchez, and B. W. Crowell (2013). On robust and reliable automated baseline corrections for strong motion seismology, *J. Geophys. Res.* **118,** no. 3, 1177–1187.

Melgar, D., B. W. Crowell, J. Geng, R. M. Allen, Y. Bock, S. Riquelme, E. M. Hill, M. Protti, and A. Ganas (2015). Earthquake magnitude calculation without saturation from the scaling of peak ground displacement, *Geophys. Res. Lett.* **42,** no. 13, 5197–5205, doi: 10.1002/2015GL064278.

Minson, S. E., J. R. Murray, J. O. Langbein, and J. S. Gomberg (2014). Real-time inversions for finite fault slip models and rupture geometry based on high-rate GPS data, *J. Geophys. Res.* **119,** no. 4, 3201–3231.

Riquelme, S., F. Bravo, D. Melgar, R. Benavente, J. Geng, S. Barrientos, and J. Campos (2016). W phase source inversion using high-rate regional GPS data for large earthquakes, *Geophys. Res. Lett.* **43,** no. 7, 3178–3185.

Ruhl, C. J., D. Melgar, R. Grapenthin, and R. M. Allen (2017). The value of real-time GNSS to earthquake early warning, *Geophys. Res. Lett.* **44,** no. 16, 8311–8319.

Satake, K., and M. Heidarzadeh (2017). A review of source models of the 2015 Illapel, Chile earthquake and insights from tsunami data, *Pure Appl. Geophys.* **174,** no. 1, 1–9.

Christine J. Ruhl
Diego Melgar[1]
Richard M. Allen
Berkeley Seismological Laboratory
University of California, Berkeley
309 McCone Hall #4760
Berkeley, California 94720-4760 U.S.A.
cruhl@berkeley.edu
rallen@berkeley.edu

Jianghui Geng
GNSS Research Center
Wuhan University
129# Luoyu Road
Wuhan 430079, China
jgeng@whu.edu.cn

Dara E. Goldberg
Yehuda Bock

Downloaded from https://pubs.geoscienceworld.org/ssa/srl/article-pdf/90/1/271/4602961/srl-2018177.1.pdf
by University of California Berkeley Library, rallen

Cecil H. and Ida M. Green Institute of Geophysics and Planetary Physics
Scripps Institution of Oceanography
University of California, San Diego
9500 Gillman Drive
La Jolla, California 92037 U.S.A.
degoldberg@ucsd.edu
ybock@ucsd.edu

Brendan W. Crowell
Department of Earth and Space Sciences
University of Washington
Seattle, Washington U.S.A.
crowellb@uw.edu

Sergio Barrientos
Sebastian Riquelme
Juan Carlos Baez
Universidad de Chile
Centro Sismológico Nacional
Santiago, Chile
sbarrien@csn.uchile.cl
sebastian@dgf.uchile.cl
jcbaez@csn.uchile.cl

Enrique Cabral-Cano
Xyoli Pérez-Campos
Universidad Nacional Autonoma de Mexico
Instituto de Geofisica
Mexico City, Mexico
ecabral@geofisica.unam.mx
xyoli@igeofisica.unam.mx

Emma M. Hill
Nanyang Technological University
Earth Observatory of Singapore
Singapore
ehill@ntu.edu.sg

Marino Protti
Universidad Nacional
Observatorio Vulcanológico y Sismológico de Costa Rica
Heredia, Costa Rica
marino.protti.quesada@una.cr

Athanassios Ganas
National Observatory of Athens
Lofos Nymphon - Thissio
PO Box 20048 - 11810
Athens, Greece
aganas@noa.gr

Mario Ruiz
Patricia Mothes
Paul Jarrín
Instituto Geofisico
Escuela Politecnica Nacional
Ladrón de Guevara E11-253 y Andalucía
Quito 170525, Ecuado
mruiz@igepn.edu.ec
pmothes@igepn.edu.ec
pjarrin@igepn.edu.ec

Jean-Mathieu Nocquet
Geoazur, IRD
Université de Nice Sophia-Antipolis
250 rue Albert Einstein - CS 10269
F 06905 SOPHIA ANTIPOLIS Cedex
France
nocquet@geoazur.unice.fr

Jean-Phillipe Avouac
Department of Geological and Planetary Sciences
California Institute of Technology
1200 E California Boulevard
Pasadena, California 91125 U.S.A.
avouac@gps.caltech.edu

Elisabetta D'Anastasio
GNS Science
1 Fairway Drive, Avalon 5010
PO Box 30-368
Lower Hutt 5040, New Zealand
E.DAnastasio@gns.cri.nz

Published Online 31 October 2018

[1] Now at Department of Earth Science, University of Oregon, 100 Cascade Hall 1272, Eugene, Oregon 97403-1272 U.S.A.

Downloaded from https://pubs.geoscienceworld.org/ssa/srl/article-pdf/90/1/271/4602961/srl-2018177.1.pdf
by University of California Berkeley Library, rallen